Applied and Computational Mechanics 5 (2011) 29–44

Numerical analysis of bypass model geometrical parameters influence on pulsatile blood flow

A. Jonášová[a,*], J. Vimmr[a], O. Bublík[a]

[a] *Faculty of Applied Sciences, University of West Bohemia, Univerzitní 22, 306 14 Plzeň, Czech Republic*

Received 5 January 2011; received in revised form 22 April 2011

Abstract

The present study is focused on the analysis of pulsatile blood flow in complete idealized 3D bypass models in dependence on three main geometrical parameters (stenosis degree, junction angle and diameter ratio). Assuming the blood to be an incompressible Newtonian fluid, the non-linear system of Navier-Stokes equations is integrated in time by a fully implicit second-order accurate fractional-step method. The space discretization is performed with the help of the cell-centred finite volume method formulated for unstructured tetrahedral grids. In order to model a realistic coronary blood flow, a time-dependent flow rate taken from corresponding literature is considered. For the analysis of obtained numerical results, special emphasis is placed on their comparison in the form of velocity isolines at several selected cross-sections during systolic and diastolic phases. The remainder of this paper is devoted to discussion of walls shear stress distribution and its oscillatory character described by the oscillatory shear index with regard to areas prone to development of intimal hyperplasia or to thrombus formation.

Keywords: bypass model, pulsatile blood flow, stenosis degree, junction angle, diameter ratio, fractional-step method, FVM

1. Introduction

One of the main problems of implanted bypass grafts is related to intimal hyperplasia, [2], an abnormal healing process occurring at the distal anastomosis. It is typical for thickening of tunica intima (the innermost layer of an artery) and after several years also for graft patency loss and bypass failure. Many clinical studies indicate the importance of hemodynamics during healing processes after serious vessel surgeries. Local hemodynamics is also hypothesized to be a trigger of several serious vascular diseases such as atherosclerosis and intimal hyperplasia, [10]. Several hemodynamical factors are currently assumed to be responsible for the activation of endothelial cells in tunica intima, [11], resulting in metabolical and morphological changes within the vessel wall. In the case of intimal hyperplasia, low and oscillating wall shear stress τ_W is often mentioned, [10], since the thickening of tunica intima is similar to the development of atherosclerotic lesions in early stages. In practice, blood's influence on the endothelial cells is often analyzed in the form of several selected hemodynamical factors such as wall shear stress (WSS) and oscillatory shear index (OSI). For more details on the theme of hemodynamical factors and their significance in connection with cardiovascular diseases and disorders see [8].

Although the understanding of hemodynamics and its influence on arterial wall morphology can be crucial for patient's survival, the actual connection between blood flow and the

*Corresponding author. Tel.: +420 377 632 397, e-mail: jonasova@kme.zcu.cz.

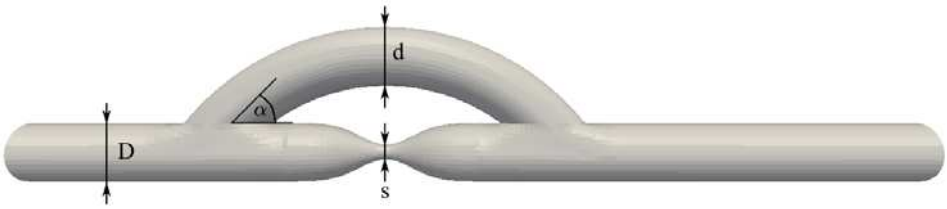

Fig. 1. Selected geometrical parameters for an idealized end-to-side bypass model with stenosed artery

occurrence of pathological changes still remains unknown. In this case, the investigation of hemodynamics in the form of numerical simulations represents one of possible contributions to the understanding of this problem. In the last decade, quite many studies dealt with the analysis of blood flow and geometry optimization, e.g., [3, 5, 7]. Considering all the surgery techniques usually used for bypass grafting of end-to-side anastomoses, it is possible to name several important geometrical parameters crucial for the resulting flow field. Beside the so-called distance of grafting (distance between the distal anastomosis and the narrowed or occluded artery part) analyzed for example in [1], following three parameters are usually mentioned.

- **Stenosis degree** characterizes the narrowing of the native artery and is stated as

$$\text{stenosis degree} = \frac{D - s}{D} \cdot 100\,\%\,,$$

  where D is the native artery diameter and s is the narrowed artery diameter, see Fig. 1. In clinical practice, it is an important indicator of arterial damage and its severity. In the case of bypass graft surgery, the degree of artery narrowing determines the need for a surgical intervention, which is usually above 70 % depending on artery damage and surgeon's experience. From published numerical studies dealing with various stenosis degrees in relation to bypass hemodynamics, it is possible to mention [5]. The authors observed hemodynamical changes for steady boundary conditions in five different bypass models (0 %, 70 %, 80 %, 90 % and 100 %) with the outcome that stenosis severity has a significant impact on the final distribution of velocity and wall shear stress within the bypass model.

- **Junction angle** (α) also known as anastomosis or bifurcation angle is the angle between native artery and implanted bypass graft, Fig. 1. The choice of the angle may be decided by the surgeon during a bypass surgery depending on the actual condition of the native artery (small angles require larger artery incision and longer suture lines). One of the first studies that investigated this geometrical parameter in a complete idealized bypass model was [7], which dealt with angles $30°$, $45°$, $60°$, $75°$ and $90°$ for steady flow conditions. The authors concluded that the angle values have a significant impact on the occurrence of secondary flows and recirculation zones in the bypass model.

- **Diameter ratio** ($D : d$) represents the ratio between the diameter of native artery D and that of bypass graft d, Fig. 1. Its importance lies in the application of grafts with adequate inner diameters so that the amount of restored blood supply to the distal part of the native artery is sufficient for downstream tissue perfusion. Although the graft diameter may seem to be one of the most optional parameters used in bypass surgery, in reality the surgeon's choice in selecting an appropriate vascular graft is limited by the performed

surgery type. For example, bypass grafting in the case of coronary arteries is currently done only with autologous arterial and venous grafts with given inner diameters. On the other hand, peripheral vascular bypass grafting is mostly carried out with synthetic grafts whose inner diameter is guaranteed by their manufacturer. Despite these limitations it is very advisable for the surgeons to be aware what the selection of inadequate graft may cause. In this regard, the authors of this paper have not be able to find a numerical study dealing with this kind of problem. A similar problem may be seen in the application of the so-called Miller cuff bypass graft mentioned, e.g., in [3], whose distal anastomosis is artificially enlarged in comparison to the native artery diameter.

Since the authors of this paper were unable to find a study that would be solely focused on the analysis of geometrical parameters influence on *pulsatile* bypass hemodynamics, the main objective of the study presented here is to perform a more in-depth comparison of geometry influence on physiological blood flow through a complete idealized end-to-side bypass model. The flow changes will be observed for three different values of stenosis degree, junction angle and diameter ratio. For results evaluation, special emphasis will be placed on the analysis of velocity distribution during the two phases of cardiac cycle (systole and diastole). Distribution of wall shear stress (WSS) and its oscillatory tendencies in the form of oscillatory shear index (OSI), [6], will be taken into account as well.

2. Problem formulation

In comparison to the majority of published studies, which modelled blood flow mainly in distal bypasses, e.g., [1, 3], this paper considers an idealized stenosed 3D bypass model with both proximal and distal parts, Fig. 1. This step is made in order to develop an adequate flow field at the distal anastomosis and also to enable us to observe flow changes inside the bypass graft in dependence on the studied geometrical parameter. For the purpose of results comparison, the bypass model proportions are set uniform regardless of the chosen geometrical parameter value, i.e., the native artery length is set to $L = 50$ mm and artery diameter is equal to $D = 3$ mm corresponding to an average right coronary artery. Taking into account the shape variability of all atherosclerotic plaques, the arterial narrowing is approximated with the help of the Gaussian function providing a smooth and realistic transition between the damaged and non-damaged native artery parts. In accordance to similar studies, e.g., [5, 7], we assume all bypass walls to be rigid and impermeable. This assumption is based on the knowledge that the majority of implanted bypass grafts is either of venous origin or is made of special synthetic materials, whose elastic properties are rather negligible, [10].

An overview of bypass model configurations studied in this paper is shown in Fig. 2. The left column represents models with various stenosis degrees (50 %, 75 % , 100 % — fully occluded native artery), the middle column stands for models with various junction angles ($\alpha = 30°$, $45°$, $70°$) and the right column shows models with various graft diameters ($D : d = 1 : 0.5; 1 : 1; 1 : 1.5$). At this point, note that in the case of configurations with 75 % stenosis, junction angle $\alpha = 45°$ and diameter ratio $D : d = 1 : 1$, the bypasses are all identical and will be later refereed to as the reference bypass model. The unstructured computational mesh for each considered bypass model configuration is generated with the help of the commercial software package Altair Hypermesh, see Fig. 3. In order to obtain grid independent results, numerical experiments were carried out for computational grids with around $150\,000$, $300\,000$ and $500\,000$ tetrahedral cells. In the end, it was stated that results computed for grids with $300\,000$ and

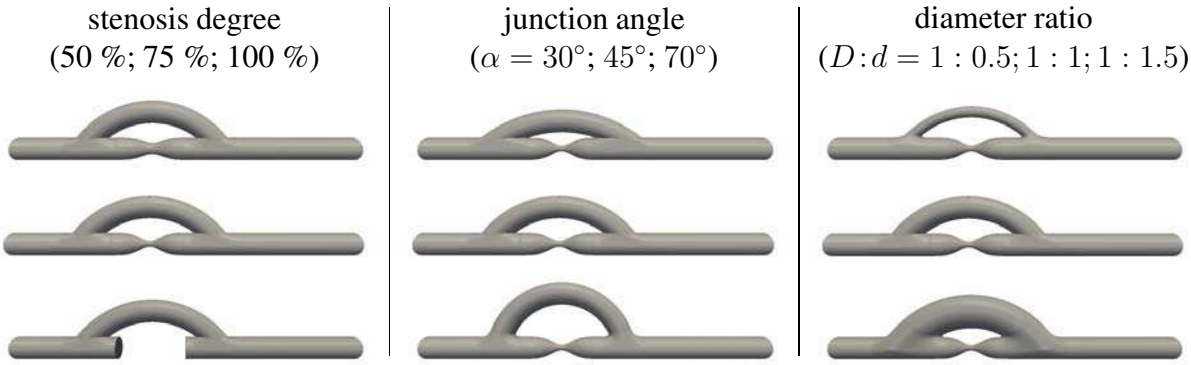

Fig. 2. Bypass model configurations with considered geometrical parameters

500 000 cells were comparable leading to the application of 300 000 cells mesh in all considered bypass configurations.

Since the aim of this paper is to investigate the problem of geometry influence on physiological bypass hemodynamics, several assumptions are made. Firstly, blood flow is modelled as an isothermal laminar pulsatile flow of incompressible Newtonian fluid with density $\varrho = 1\,060\,\mathrm{kg}\cdot\mathrm{m}^{-3}$ and dynamic viscosity $\eta = 3.45\cdot 10^{-3}\,\mathrm{Pa}\cdot\mathrm{s}$. Regarding the supposed blood's Newtonian behaviour, the authors of this paper have taken into account conclusions resulting from their previous numerical simulations of non-Newtonian blood flow, [13, 14]. For steady flow conditions, it was stated that the occurrence of non-Newtonian effects in coronary bypass models is minimal. Hence, blood may be treated as Newtonian fluid in the case of coronary bypasses. The second assumption made in this paper is related to the prescription of realistic blood flow conditions, since blood flow in human arteries is always pulsatile. The problem is approached by considering a time-dependent inlet flow rate $Q(t)$, Fig. 4. The data are taken from [1] and should correspond to flow rate values measured in the right coronary artery during rest. For the purpose of numerical simulations, the flow rate is prescribed in the form of following Fourier series

$$Q(t) = A_0 + \sum_{k=1}^{5} A_k \cos\left(k\omega t - \varphi_k\right), \tag{1}$$

where $\omega = 2\pi/T$ is the angular frequency determined from cardiac period $T = 1.68\,\mathrm{s}$, $A_0 = 65.07\,\mathrm{ml}\cdot\mathrm{min}^{-1}$ represents the steady flow rate component and A_k and $\varphi_k,\ k = 1,\ldots,5$ are the amplitude and the phase angle, respectively.

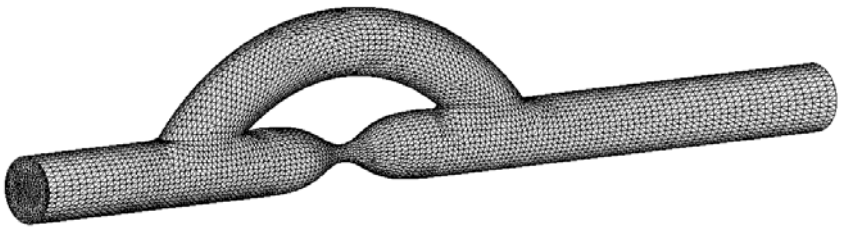

Fig. 3. Unstructured tetrahedral computational mesh — reference bypass model

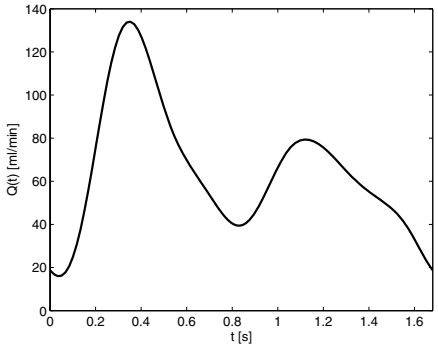

k	A_k [ml · min^{-1}]	φ_k [rad]
1	18.149	1.944
2	34.828	2.836
3	12.329	−2.124
4	9.107	−1.875
5	2.944	−0.447

Fig. 4. Prescribed time-dependent inlet flow rate $Q(t)$ corresponding to the right coronary artery during rest, [1], and overview of amplitude and phase values used in the Fourier series (1)

3. Mathematical model and numerical method

Let us consider a time interval $(0, \mathcal{T})$, $\mathcal{T} > 0$ and a bounded computational domain $\Omega \subset \mathbf{R}^3$ with boundary $\partial\Omega = \partial\Omega_I \cup \partial\Omega_O \cup \partial\Omega_W$, where $\partial\Omega_I$, $\partial\Omega_O$ and $\partial\Omega_W$ denote the inlet, the outlet and the rigid walls, respectively. The governing equations describing the pulsatile motion of blood in the given computational domain Ω constitute the non-linear system of the incompressible Navier-Stokes (NS) equations written in the non-dimensional form

$$\frac{\partial v_j}{\partial y_j} = 0\,, \tag{2}$$

$$\frac{\partial v_i}{\partial t} + \frac{\partial}{\partial y_j}(v_i v_j) + \frac{\partial p}{\partial y_i} = \frac{1}{Re}\,\frac{\partial^2 v_i}{\partial y_j \partial y_j} \quad \text{for } i,j = 1,2,3 \tag{3}$$

in the space-time cylinder $\Omega_T = \Omega \times (0, \mathcal{T})$, where $t \in (0, \mathcal{T})$ is the time, v_i is the i-component of the velocity vector $\boldsymbol{v} = [v_1, v_2, v_3]^T$ corresponding to the Cartesian coordinate $y_i \in \Omega$, p is the pressure, ϱ and η are the density and the molecular viscosity of blood, respectively. The reference Reynolds number is given as $Re = U_{ref} D_{ref} \varrho/\eta = 141.4$, where $U_{ref} = 0.153\,\mathrm{m\cdot s^{-1}}$ is the reference velocity corresponding to the average inlet velocity and D_{ref} is the reference length equal the native artery diameter $D = 3\,\mathrm{mm}$.

Considering a discretized 3D computational domain in the form of an unstructured tetrahedral grid with control volumes Ω_k, a hybrid grid system is applied for all calculations, [4]. Beside the values of pressure and velocity vector components computed in cell-centers, the hybrid grid system defines also a normal velocity V_m at the cell-faces. For the m-th face Γ_k^m of the control volume Ω_k, the normal velocity is calculated as $V_m = v_{im} \cdot {}^i n_k^m$, where $\boldsymbol{n}_k^m = [{}^1n_k^m, {}^2n_k^m, {}^3n_k^m]^T$ is the outward unit vector normal to the cell face Γ_k^m, v_{im} are the velocity components at the m-th face Γ_k^m of the control volume Ω_k.

For time discretization of the non-linear system of the Navier-Stokes equations (2)–(3), a fully implicit second order accurate fractional step algorithm is used, [4]. The application of the implicit second order Crank-Nicolson scheme to the convective and viscous terms and the implicit Euler scheme to the pressure term in (3) leads to

$$\frac{v_i^{n+1} - v_i^n}{\Delta t} + \frac{1}{2}\frac{\partial}{\partial y_j}\left(v_i^{n+1} v_j^{n+1} + v_i^n v_j^n\right) = -\frac{\partial p^{n+1}}{\partial y_i} + \frac{1}{2Re}\,\frac{\partial^2}{\partial y_j \partial y_j}\left(v_i^{n+1} + v_i^n\right)\,, \tag{4}$$

where $\Delta t = t_{n+1} - t_n$ is the time step between time levels t_n and t_{n+1}. Next, the convective

terms in (4) are linearized with second order accuracy

$$v_i^{n+1}v_j^{n+1} = v_i^{n+1}v_j^n + v_i^n v_j^{n+1} - v_i^n v_j^n + \mathcal{O}(\Delta t^2)\,. \tag{5}$$

The subtitution of (5) into (4) gives a linearized system of partial differential equations

$$\frac{v_i^{n+1}-v_i^n}{\Delta t} + \frac{1}{2}\frac{\partial}{\partial y_j}\left(v_i^{n+1}v_j^n + v_i^n v_j^{n+1}\right) = -\frac{\partial p^{n+1}}{\partial y_i} + \frac{1}{2Re}\frac{\partial^2}{\partial y_j \partial y_j}\left(v_i^{n+1} + v_i^n\right)\,. \tag{6}$$

Finally, the application of the fractional step algorithm yields following equations

$$\frac{\hat{v}_i - v_i^n}{\Delta t} + \frac{1}{2}\frac{\partial}{\partial y_j}\left(\hat{v}_i v_j^n + v_i^n \hat{v}_j\right) = -\frac{\partial p^n}{\partial y_i} + \frac{1}{2Re}\frac{\partial^2}{\partial y_j \partial y_j}\left(\hat{v}_i + v_i^n\right)\,, \tag{7}$$

$$\frac{\partial^2 \Psi}{\partial y_i \partial y_i} = \frac{\partial \hat{v}_i}{\partial y_i}\,, \tag{8}$$

$$p^{n+1} = p^n + \frac{1}{\Delta t}\Psi\,, \tag{9}$$

$$v_i^{n+1} = \hat{v}_i - \frac{\partial \Psi}{\partial y_i}\,, \tag{10}$$

where Ψ is the pressure correction function and $\hat{v}_i$ are the velocity vector components introduced by the numerical method.

For spatial discretization of the system of equations (7)–(10), the cell-centered finite volume method is used. After several mathematical operations, following system of algebraic equations can be obtained

$$\begin{aligned}(\delta\hat{v}_i)_k &+ \frac{\Delta t}{2|\Omega_k|}\sum_{m=1}^{4}\left(\delta\hat{v}_{i\,m}V_m^n + v_{i\,m}^n \cdot {}^j n_k^m \;\delta\hat{v}_{j\,m} + 2v_{i\,m}^n V_m^n\right)|\Gamma_k^m| = \\ &-\frac{\Delta t}{|\Omega_k|}\sum_{m=1}^{4} p_m^n \cdot {}^i n_k^m |\Gamma_k^m| + \frac{\Delta t}{2Re|\Omega_k|}\sum_{m=1}^{4}\frac{\partial}{\partial n_k^m}\left(\delta\hat{v}_{i\,m} + 2v_{i\,m}^n\right)|\Gamma_k^m|\,,\end{aligned} \tag{11}$$

$$\sum_{m=1}^{4}\frac{\partial\Psi}{\partial n_k^m}|\Gamma_k^m| = \sum_{m=1}^{4}\hat{v}_{i\,m}\cdot {}^i n_k^m|\Gamma_k^m| \equiv \sum_{m=1}^{4}\hat{V}_m|\Gamma_k^m|\,, \tag{12}$$

$$\left(p^{n+1}\right)_k = (p^n)_k + \frac{1}{\Delta t}(\Psi)_k\,, \tag{13}$$

$$(v_i^{n+1})_k = (\hat{v}_i)_k - \frac{1}{|\Omega_k|}\sum_{m=1}^{4}\Psi_m \cdot {}^i n_k^m |\Gamma_k^m|\,, \tag{14}$$

$$V_m^{n+1} = \hat{V}_m - \frac{\partial\Psi}{\partial n_k^m}\,, \tag{15}$$

where $\delta\hat{v}_i = \hat{v}_i - v_i^n$, $\hat{V}_m$ is the hat velocity normal to the m-th cell face, $|\Gamma_k^m|$ is the area of the m-th face Γ_k^m of the control volume Ω_k, $|\Omega_k|$ is the volume of the control volume Ω_k, ${}^i n_k^m$ are the components of the outward unit vector normal to the cell face Γ_k^m. The adding of equation (15) to the system of equations (11)–(14) helps to suppress unwanted oscillations in the pressure field and to satisfy the continuity equation. Namely, it can be shown that the calculated velocity components $\left(v_i^{n+1}\right)_k$ do not generally satisfy the continuity equation at the $(n+1)$-th time level.

On the other hand, the normal velocities V_m^{n+1} give a divergence-free velocity field. Therefore, normal velocity values V_m^{n+1} determined in (15) are used in (11) and (12) at the next time level instead of V_m^n.

For evaluation of quantities and their derivatives at the m-th cell face Γ_k^m of the control volume Ω_k in (11)–(15), a second order interpolation method is used, [12]. Let us consider an arbitrary quantity Φ in the computed flow field. Its value Φ_m at the m-th face Γ_k^m can be determined using the second order interpolation method as

$$\Phi_m = (\Phi)_k + \frac{(\Phi)_{l_m} - (\Phi)_k}{\gamma_k + \gamma_{l_m}} \cdot \gamma_k = \frac{\gamma_{l_m}(\Phi)_k + \gamma_k(\Phi)_{l_m}}{\gamma_k + \gamma_{l_m}}, \tag{16}$$

where γ_k and γ_{l_m} are the minimal distances to the cell-face Γ_k^m from cell-centers S_k and S_{l_m} of the neighbouring control volumes Ω_k and Ω_{l_m}, respectively. The derivative of the quantity Φ in the direction of the unit outer vector $\boldsymbol{n}_k^m$ normal to the m-th face Γ_k^m of the control volume Ω_k can be approximated as

$$\frac{\partial \Phi}{\partial n_k^m}\Big|_{\Gamma_k^m} \approx \frac{(\Phi)_{l_m} - (\Phi)_k}{\gamma_k + \gamma_{l_m}}\,. \tag{17}$$

Regarding the application of boundary conditions, following approach has to be adopted. At the inlet, velocity vector components v_{iI} and zero pressure derivative $\frac{\partial p}{\partial n} = 0$ are prescribed. At the outlet, a known pressure p_O is given leading to the condition

$$-p\boldsymbol{n} + \frac{1}{Re} \cdot \frac{\partial \boldsymbol{v}}{\partial n} = -p_O \boldsymbol{n}\,. \tag{18}$$

At the solid walls, non-slip boundary condition $\boldsymbol{v} = \boldsymbol{0}$ and zero pressure derivative $\frac{\partial p}{\partial n} = 0$ is considered. For the numerical solution of the Poisson equation (12), zero pressure correction derivative $\frac{\partial \Psi}{\partial n} = 0$ at the inlet and at the solid walls are applied. In order to keep the required pressure value $p = p_O$ at the outlet, Dirichlet boundary condition $\Psi = 0$ is prescribed. The correction of the normal velocity (15) guarantees the satisfaction of the continuity equation for all control volumes except the ones with a face lying at the outlet boundary $\partial\Gamma_O$. In this case, normal velocity values have to be controlled so that the computed velocity field satisfies the continuity equation within these control volumes.

Taking into account boundary conditions mentioned above, equation (11) leads to the system of linear algebraic equations $\boldsymbol{A}\boldsymbol{x} = \boldsymbol{b}$ with sparse matrix $\boldsymbol{A}$ of order $3N_{CV}$, where N_{CV} is the total number of control volumes. Similarly, the Poisson equation for the pressure correction (12) with implemented boundary conditions leads to the system of linear algebraic equations $\tilde{\boldsymbol{A}}\tilde{\boldsymbol{x}} = \tilde{\boldsymbol{b}}$ with sparse matrix $\tilde{\boldsymbol{A}}$ of order N_{CV}. For the numerical solution of both these systems, the BICGSTAB iterative method with the incomplete LU preconditioner implemented in the UMFPACK library is used.

4. Numerical results and discussion

Since the objects of interest in this paper are three different geometrical parameters considered in similar bypass model configurations, only one version of unsteady boundary conditions is prescribed at corresponding computational domain boundaries:

- *inlet* $\partial\Omega_I$ — fully developed time-dependent velocity profile

$$v_{1I}(r,t) = \frac{8Q(t)}{\pi D^2}\left[1 - \left(\frac{2r}{D}\right)^2\right], \quad v_{2I} = v_{3I} = 0 \text{ m} \cdot \text{s}^{-1},$$

where $r = \sqrt{y_2^2 + y_3^2}$ denotes the distance from artery center-line, D is the diameter of the coronary native artery and $Q(t)$ is the time-dependent flow rate, Fig. 4;

- *outlet* $\partial\Omega_O$ — constant pressure $p_O = 12\,\text{kPa}$ corresponding to average arterial pressure;
- *impermeable and rigid walls* $\partial\Omega_W$ — non-slip boundary condition, i.e., $\boldsymbol{v} = \boldsymbol{0}$.

The application of fully developed velocity profile instead of a commonly used Womersley velocity profile results from prescribed inlet values. According to [9], the oscillatory Womersley velocity profile may be satisfactorily approximated by a time-varying parabolic velocity profile, also often denoted as 'quasi-steady', when the Womersley number of the pulsatile flow is sufficiently low ($Wo < 3$). In our case, the Womersley number is stated as $Wo = 0.5D\sqrt{\omega\varrho/\eta} = 1.61$ and enables us to prescribe the velocity profile mentioned above.

4.1. Velocity distribution

For a better comparison between each considered bypass model, velocity isolines at five different cross-sections are presented for various stenosis degrees, junction angles and diameter ratios in Table 1, Table 2 and Table 3, respectively. The upper part of each table shows results from systolic phase ($t_1 = 0.34\,\text{s}$) and the lower part from diastolic phase ($t_2 = 1.12\,\text{s}$) of the cardiac cycle, Fig. 5. The selection of all displayed cross-sections was made in order to take the flow character of each bypass configuration and their geometrical differences into account. In this regard, not every cross-section is located at the same distance from the inlet. On the other hand, all cross-sections should be approximately situated at following positions. The first cross-section denoted as A should show the flow field before the arterial narrowing and together with B, which is located near the graft inlet, should present the proximal bypass hemodynamics. On the other hand, the downstream hemodynamics near the distal anastomosis, which is of main interest in this paper, should be given by cross-sections C, D and E.

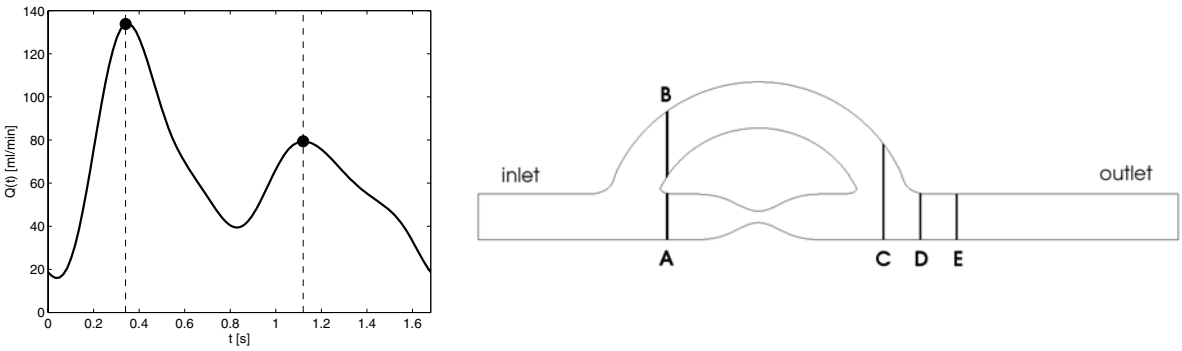

Fig. 5. Time instants $t_1 = 0.34\,\text{s}$ and $t_2 = 1.12\,\text{s}$ used for visualization of velocity isolines at selected cross-sections A–E along the idealized 3D bypass model

Despite the different maximum velocities during systolic and diastolic phases, the flow fields shown in Table 1 for the three stenosis degrees do not appear to be too dissimilar in dependence on the current inlet velocity. On the other hand, the comparison between each bypass configuration indicates several hemodynamical changes regardless of the current time instant. For example, the region around the arterial narrowing (cross-section A) in the case of the 100 % stenosis (occlusion) is filled with a large and relatively high-velocity recirculation zone in comparison to other bypasses. Another more distinct difference is the skewed shape of velocity profiles at

Table 1. Velocity isolines at cross sections A–E for various stenosis degrees, Fig. 5

stenosis degree	$t_1 = 0.34\,\mathrm{s}$					
	A	B	C	D	E	
50 %	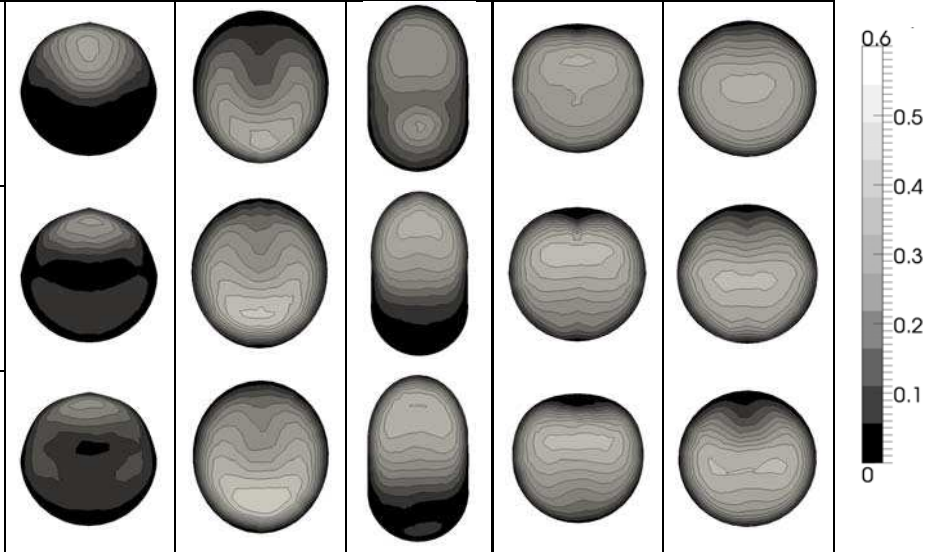					
75 % (ref.)						
100 %						
stenosis degree	$t_2 = 1.12\,\mathrm{s}$					
	A	B	C	D	E	
50 %	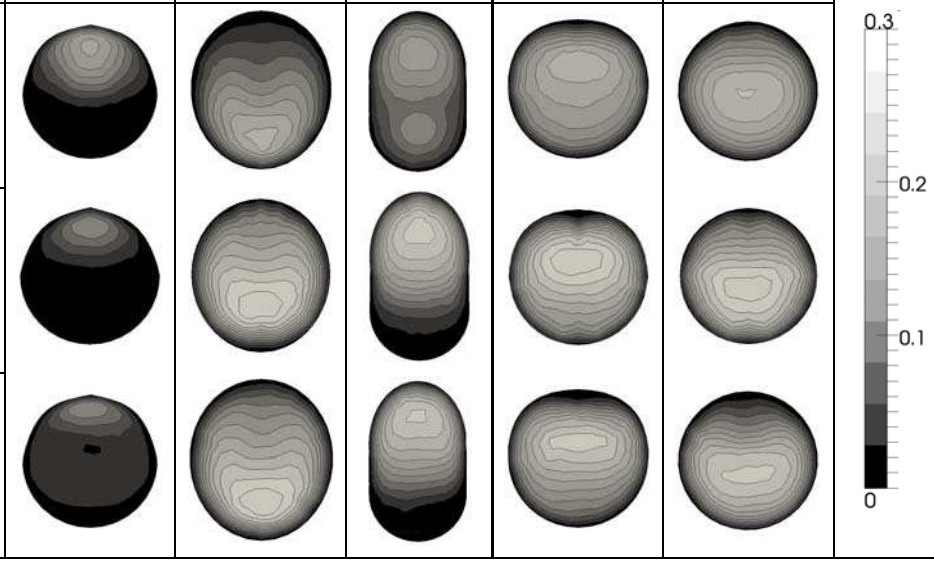					
75 % (ref.)						
100 %						

the graft inlet (cross-section B) and downstream from the distal anastomosis (cross-section C). In order to better understand the connection between stenosis degree and hemodynamics, the authors of this paper deem it necessary to present corresponding longitudinal sections of the three considered bypass models, Fig. 6a-c. At first sight, it is apparent that the overall blood flow in the 50 % stenosis configuration is mostly directed towards the stenosis, leading to a relatively low-velocity flow in the bypass graft and to a development of recirculation zones near the graft inlet, Fig. 6b. Some improvements can be found in the reference model with typical recirculation zones around the stenosis, Fig. 6a. With regard to the complete stream redirection in the case of the occluded bypass model, Fig. 6c, several small flow disturbances are visible in the vicinity of both anastomosis regions.

As to the junction angle influence on the resulting flow field, Table 2, once again no distinct differences between both cardiac phases are observed. More important in this regard seems to

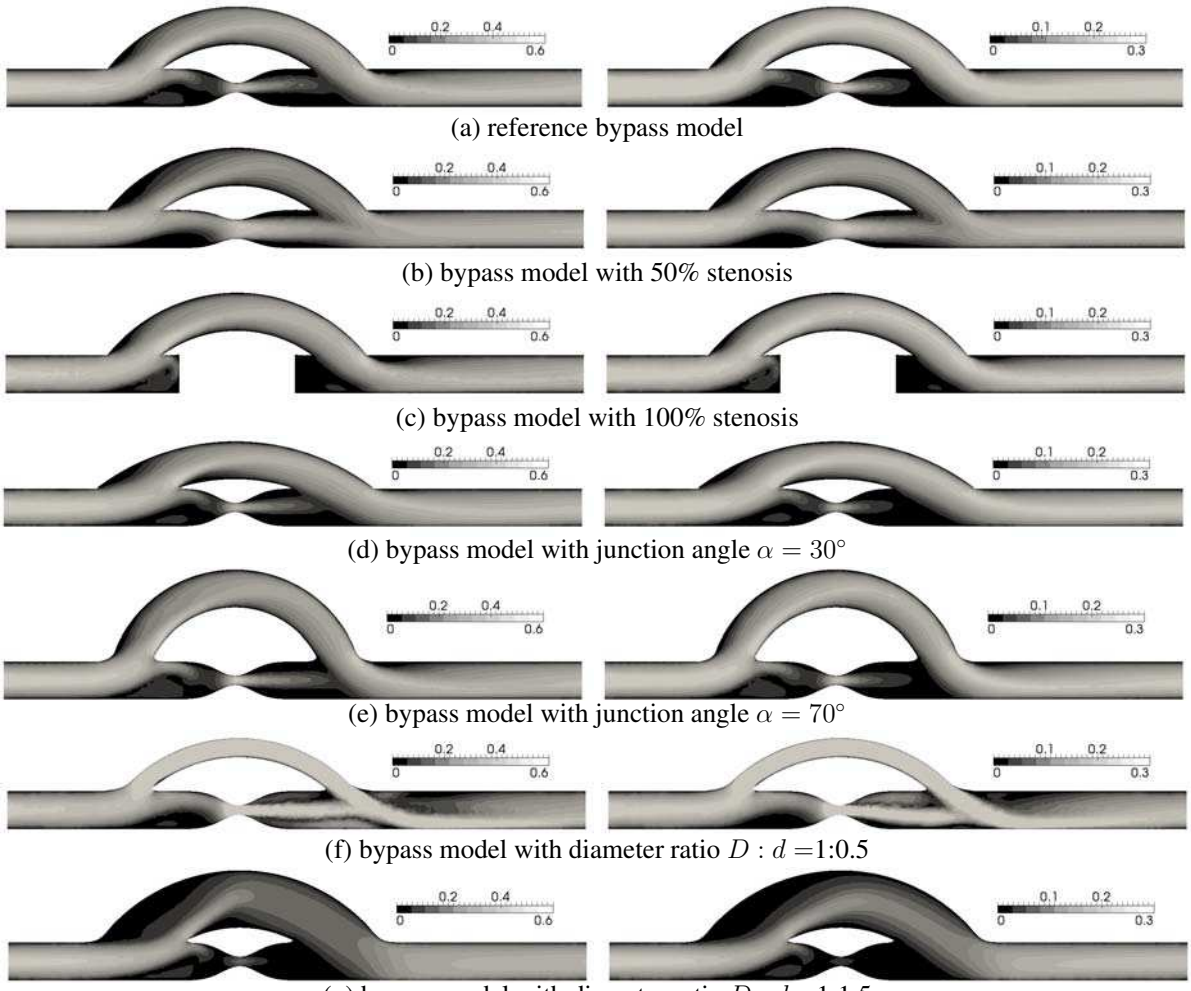

(a) reference bypass model

(b) bypass model with 50% stenosis

(c) bypass model with 100% stenosis

(d) bypass model with junction angle $\alpha = 30°$

(e) bypass model with junction angle $\alpha = 70°$

(f) bypass model with diameter ratio $D : d$ =1:0.5

(g) bypass model with diameter ratio $D : d$ =1:1.5

Fig. 6. Distribution of velocity magnitude $|\boldsymbol{v}|$ $[\mathrm{m} \cdot \mathrm{s}^{-1}]$ in the longitudinal section through all considered bypass model configurations at times $t_1 = 0.34\,\mathrm{s}$ (*left*) and $t_2 = 1.12\,\mathrm{s}$ (*right*)

be the occurrence of secondary flows and 'M'-shaped velocity profiles inside the bypass graft, especially in the $70°$ configuration (cross-section B). In comparison to previous results, the junction angle influence seems to be mostly limited to regions around both anastomoses (cross-sections B and C). In this case, the hemodynamics changes have the form of sudden stream redirections and occurrence of several recirculation zones as is apparent from longitudinal sections shown in Fig. 6d–e. Referring to the $30°$ and $45°$ configurations, the small angle model indicates minimal improvement of the overall bypass flow field in comparison to the reference model, e.g., cross-sections C and D in Table 2 or Fig. 6a and 6d. On the other hand, the $70°$ model leads to the worst possible velocity distribution within the three considered angle configurations, Fig. 6e. The presence of relatively high-velocity recirculation zones (cross-section A) and the occurrence of strong secondary flows (B and E) is rather undesirable.

From all geometrical parameters considered in this paper, the diameter ratio is probably the most interesting one in relation to the resulting velocity distribution, Table 3. The main reason for the non-uniform colorbars at both time instants lies in the maximum velocity observed in the case of the bypass model, whose graft has the diameter equal to the native artery radius ($D : d = 1 : 0.5$). Since the decrease of cross-sectional area within this model entails a considerate increase in the velocity magnitude (up to $1.8\,\mathrm{m} \cdot \mathrm{s}^{-1}$ during systole), both colorbars

Table 2. Velocity isolines at cross sections A–E for various junction angles α, Fig. 5

junction angle	$t_1 = 0.34\,\mathrm{s}$					
	A	B	C	D	E	
30°	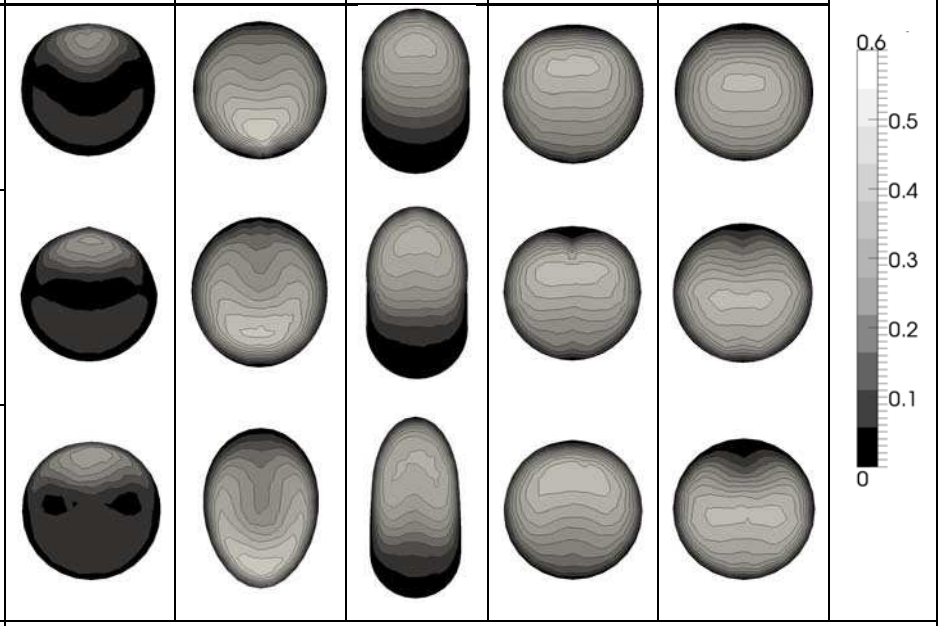					
45° (ref.)						
70°						
junction angle	$t_2 = 1.12\,\mathrm{s}$					
	A	B	C	D	E	
30°	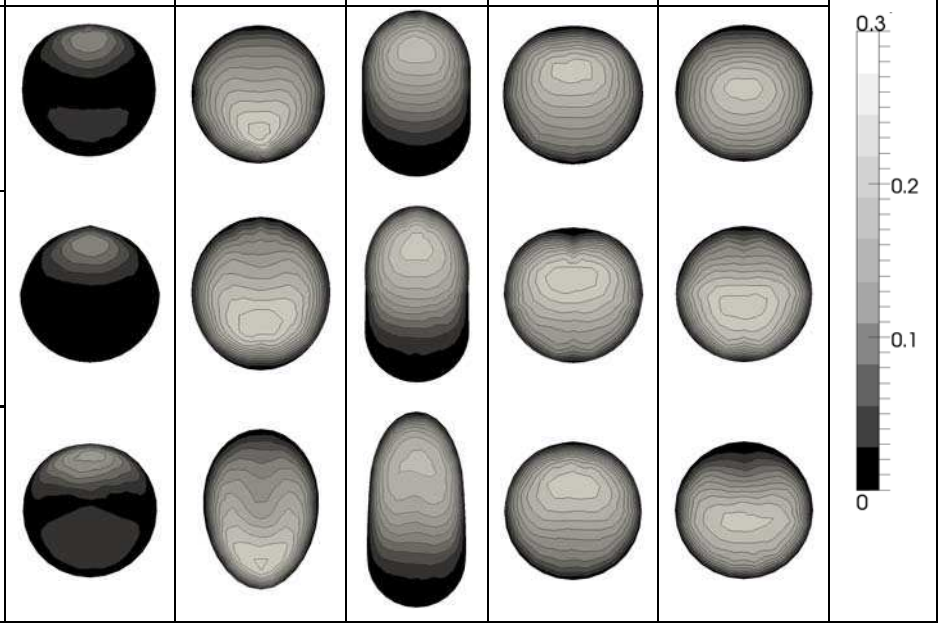					
45° (ref.)						
70°						

were chosen as non-uniform in order to capture the much lower velocities in the two remaining bypass configurations. For a better understanding, the authors of this paper present beside the cross-sections also the longitudinal sections through both small and large graft diameter models in Fig. 6f–g. Comparing the flow fields obtained for the three graft diameters, it is possible to deduce that the small diameter model gives the worst results presented for the distal anastomosis yet. The strongly disturbed and non-uniform hemodynamics in this bypass part is very well apparent from cross-sections C–E in Table 3 or from Fig. 6f. On the other hand, the large graft diameter configuration seems to be typical for relatively uniform flow field consisting of blunt velocity profiles (cross-sections C–E). Considerable disadvantage of this bypass geometry is

Table 3. Velocity isolines at cross sections A–E for various diameter ratios $D : d$, Fig. 5

diameter ratio	$t_1 = 0.34\,\mathrm{s}$					
	A	B	C	D	E	
1 : 0.5						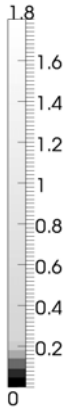
1 : 1 (ref.)						
1 : 1.5						
diameter ratio	$t_2 = 1.12\,\mathrm{s}$					
	A	B	C	D	E	
1 : 0.5						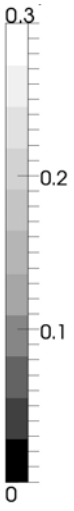
1 : 1 (ref.)						
1 : 1.5						

also the large recirculation zone that prevails during the whole cardiac cycle in the first third of the bypass graft, Fig. 6g, and is also apparent from cross-section B in Table 3.

4.2. WSS and OSI distributions

In this section, only the most interesting numerical results of WSS and OSI are going to be shown and discussed. For the WSS distribution at two time instances, the selected bypass model configurations are the reference model, the model with junction angle $\alpha = 70°$ and lastly the model with diameter ratio $D : d = 1 : 1.5$, Fig. 7a–c. For the OSI distribution, the reference model, the model with 50 % stenosis and the models with diameter ratios $D : d = 1 : 0.5$ and $D : d = 1 : 1.5$ are chosen, Fig. 8a–d. However, before the results discussion, it is appropriate

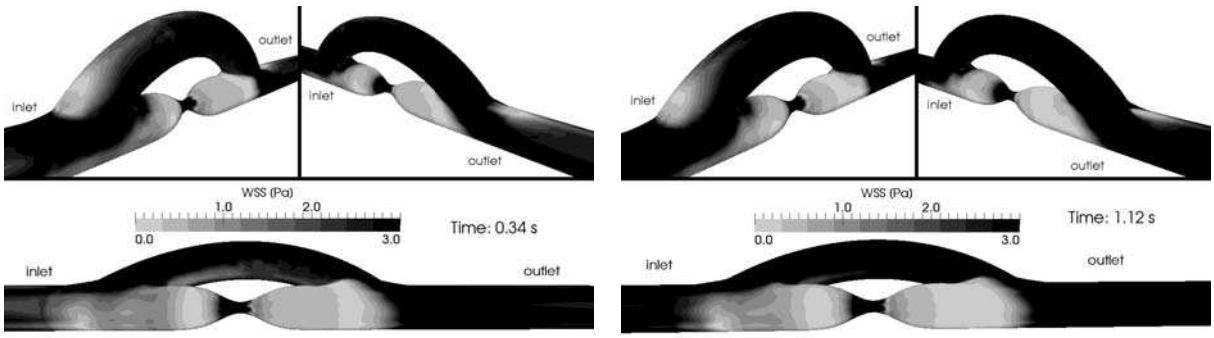

(a) reference bypass model (75 % stenosis, $\alpha = 45°$, $D : d = 1 : 1$)

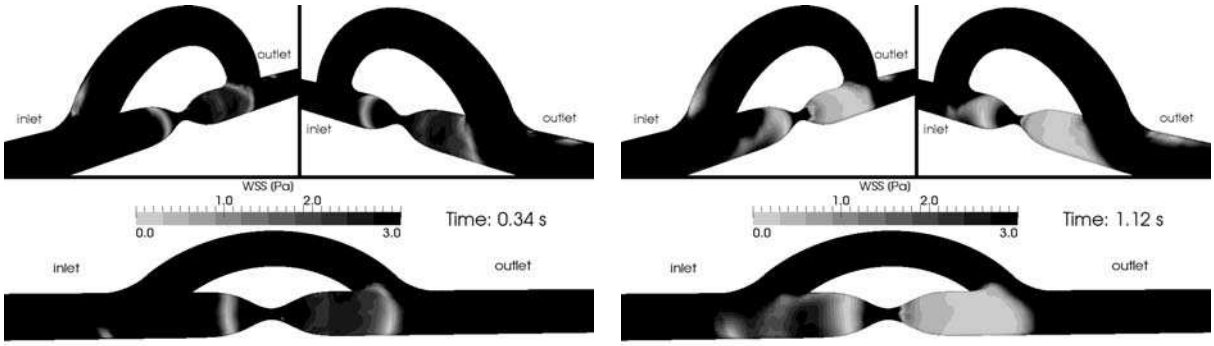

(b) bypass model with junction angle $\alpha = 70°$

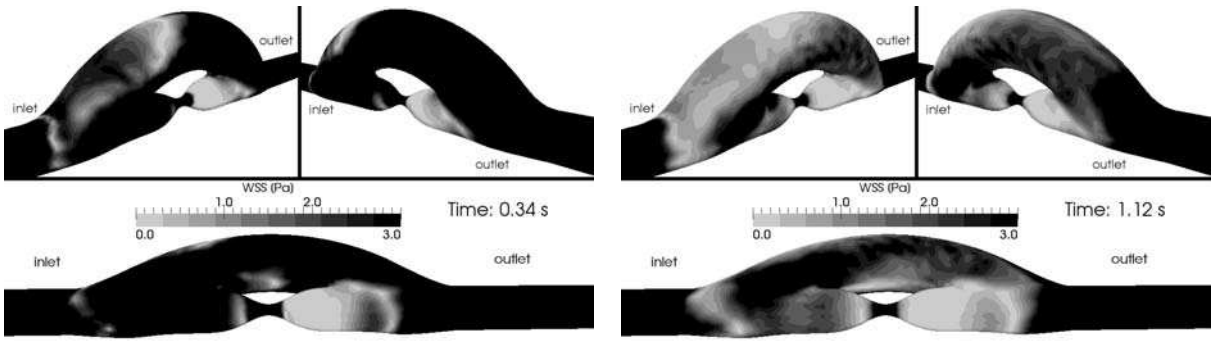

(c) bypass model with diameter ratio $D : d = 1 : 1.5$

Fig. 7. WSS distribution for three different bypass model configurations at times $t_1 = 0.34\,\mathrm{s}$ (*left*) and $t = 1.12\,\mathrm{s}$ (*right*)

to mention the definition of OSI used in this paper, which is consistent with its introduction by Ku et al. in [6],

$$OSI = \frac{1}{2}\left(1 - \frac{\left|\int_0^T \boldsymbol{\tau}_W \mathrm{d}t\right|}{\int_0^T |\boldsymbol{\tau}_W|\,\mathrm{d}t}\right). \tag{19}$$

Since low WSS values are known to negatively influence the vessel wall morphology and are, therefore, of interest here, all ranges in Fig. 7 are lowered to values between $0 \div 3\,\mathrm{Pa}$. This way, several areas within the bypass model may be denoted as to be prone to the development of atherosclerotic lesion (stenosis region) or intimal hyperplasia (proximal and distal anastomoses). The most interesting WSS distribution is shown for the large graft diameter model, Fig. 7c, whose graft walls are exposed to low WSS most of the cardiac cycle and, therefore,

may significantly enhance the risk of unwanted wall remodelling. The oscillatory character of WSS within one cardiac cycle described by OSI validates the assumption that the negative stimulation of vessel wall is concentrated to the stenosis region regardless of the actual bypass geometry, Fig. 8. Considering the risk of intimal hyperplasia development at proximal and distal anastomoses, the most prone geometries seem to be the models with diameter ratios $D : d = 1 : 0.5$ and $D : d = 1 : 1.5$, Fig. 8c–d.

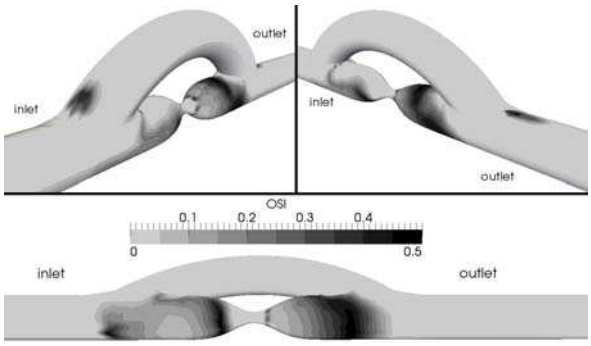

(a) reference bypass model

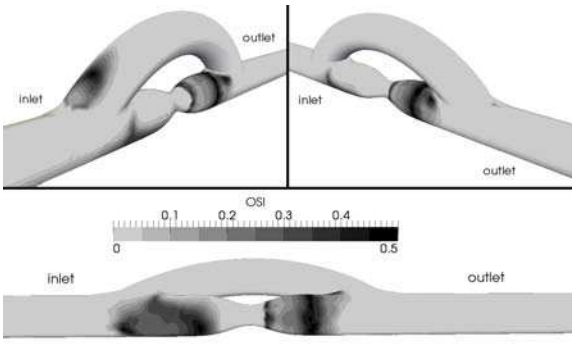

(b) bypass model with 50 % stenosis

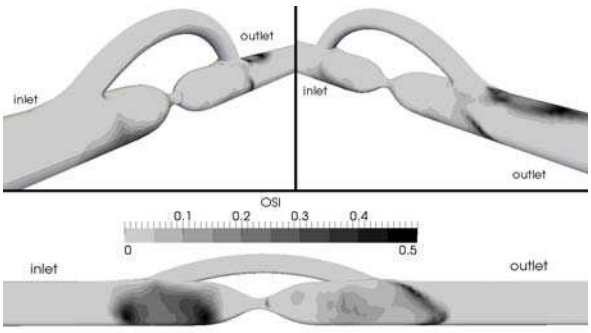

(c) bypass model with $D : d = 1 : 0.5$

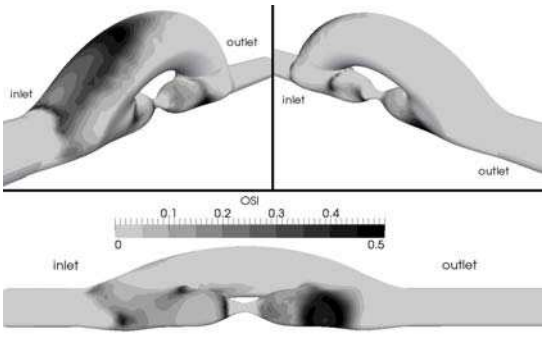

(d) bypass model with $D : d = 1 : 1.5$

Fig. 8. OSI distribution for four different bypass model configurations

5. Conclusion

The main objective of this paper was focused on the analysis of end-to-side bypass hemodynamics in dependence on three significant geometrical parameters (stenosis degree, junction angle and diameter ratio) by prescribing unsteady boundary conditions corresponding to physiological pulsatile blood flow. Special emphasis was placed on the application of own developed incompressible NS solver based on the fully implicit fractional-step method and the cell-centred finite volume method for unstructured tetrahedral grids. In comparison to their previous studies dealing with steady non-Newtonian blood flow, [13, 14], the authors dealt with the analysis of unsteady Newtonian blood flow.

The numerical results obtained for three different stenosis degrees showed the importance of residual blood flow through the arterial stenosis and its influence on the overall bypass hemodynamics. For example, the blood flow observed in the graft of the 50 % stenosis bypass configuration during the cardiac cycle showed a hemodynamics prone to thrombus formation, which after several months would lead to complete graft closure. Therefore, an graft implantation at this stage would in most cases result in an unsuccessful surgery. On the other hand,

a bypass with occluded native artery showed a relatively uniform flow field, whose only disadvantage lies in a possible red blood cells damage due to stream impact on the proximal part of the atherosclerotic lesion during systole. In the case of the junction angle $30°$, small flow field improvements were observed in comparison to the reference bypass model with $\alpha = 45°$. However, the main disadvantage of all small angle bypasses can be seen in the need for a longer suture line resulting in a serious artery damage during surgery. The presence of several recirculation zones near both anastomoses for the $70°$ configuration may enhance the risk of blood cell accumulation and possibly lead to thrombus formation in corresponding bypass parts. Probably the most interesting results were obtained by varying the graft diameter d in comparison to the constant native artery diameter D. Considering the graft cross-sectional area in the bypass model with diameter ratio $D : d = 1 : 0.5$, the considerable velocity increase, especially during systole, produced a strongly disturbed flow field with several high-velocity recirculation zones near the distal anastomosis. Therefore, it is possible to declare this bypass configuration as one with very high probability of damage and accumulation of red blood cells with very high risk of thrombus formation. On the other hand, the bypass model with large graft diameter ($D : d = 1 : 1.5$) showed relatively undisturbed flow field. The only and probably very significant exception could be found in the first third of the graft, where a large low-velocity recirculation zone prevailed during the whole cardiac cycle. From the biomechanical point of view, the corresponding WSS and OSI distribution for this bypass configuration led us to the assumption that the inadequate velocity distribution near the proximal anastomosis may very well trigger unwanted changes in the vessel wall morphology and so enhance the risk of intimal hyperplasia development. The risk of blood cell accumulation inside the bypass graft is also not negligible.

Taking all the observations into account, each described bypass configuration seems to be favourable in some way — be it adequate WSS and OSI values or uniform velocity distribution during the cardiac cycle. In general, the most optimal flow field was achieved for the reference bypass model with average values of stenosis degree (75 %), junction angle ($45°$) and diameter ratio ($D = d$). The authors of this paper are, however, convinced that a more favourable flow field could be achieved for the complete bypass model by considering a small modification in the graft geometry. Namely, a graft with gradually increasing diameter would combine the advantages of small diameter graft at the proximal anastomosis and the advantages of the large diameter one at the distal anastomosis.

By presenting hemodynamics analysis in a complete idealized bypass model for various geometrical parameters, the authors of this paper would like to finish their previous research in the field of hemodynamics for this type of bypass models. In the future, their approach should be mainly focused on modelling of blood flow in patient-specific bypass models reconstructed from CT data.

Acknowledgements

This investigation was supported by the research project MSM 4977751303 of the Ministry of Education, Youth and Sports of the Czech Republic and by the internal student grant project SGS-2010-077 of the University of West Bohemia.

References

[1] Bertolotti, C., Deplano, V., Fuseri, J., Dupouy, P., Numerical and experimental model of post-operative realistic flows in stenosed coronary bypasses, Journal of Biomechanics 34 (8) (2001) 1 049–1 064.

[2] Haruguchi, H., Teraoka, S., Intimal hyperplasia and hemodynamic factors in arterial bypass and arteriovenous grafts: a review, Journal of Artificial Organs 6 (4) (2003) 227–235.

[3] Henry, F. S., Küpper, C., Lewington, N. P., Simulation of flow through a Miller cuff bypass graft, Computer methods in Biomechanics and Biomedial Engineering 5 (3) (2002) 207–217.

[4] Kim, D., Choi, H., A second-order time-accurate finite volume method for unsteady incompressible flow on hybrid unstructured grids, Journal of Computational Physics 162 (2) (2000) 411–428.

[5] Ko, T. H., Ting, K., Yeh, H. C., Numerical investigation on flow fields in partially stenosed artery with complete bypass graft: An in vitro study, International Communications in Heat and Mass Transfer 34 (6) (2007) 713–727.

[6] Ku, D. N., Giddens, D. P., Zarins, C. K., Glagov, S., Pulsatile flow and atherosclerosis in the human carotid bifurcation – Positive correlation between plaque location and low oscillating shear stress, Arteriosclerosis, Thrombosis, and Vascular Biology 5 (3) (1985) 293–302.

[7] Lee, D., Su, J. M., Liang, H. Y., A numerical simulation of steady flow fields in a bypass tube, Journal of Biomechanics 34 (11) (2001) 1 407–1 416.

[8] Kleinstreuer, C., Buchanan, J. R., Lei, M., Truskey, G. A., Computational analysis of particle-hemodynamics and prediction of the onset of arterial diseases, In Biomechanical Systems: Techniques and Applications, Volume II: Cardiovascular Techniques, Cornelius T. Leondes (editor), CRC Press, New York, 2000.

[9] Loudon, C., Tordesillas, A., The use of the dimensionless Womersley number to characterize the unsteady nature of internal flow, Journal of Theoretical Biology 191 (1) (1998) 63–78.

[10] Loth, F., Fischer, P. F., Bassiouny, H. S., Blood flow in end-to-side anastomoses, Annual Review of Fluid Mechanics 40 (2008) 367–393.

[11] Malek, A. M., Izumo, S., Mechanism of endothelial cell shape change and cytoskeletal remodeling in response to fluid shear stress, Journal of Cell Science 109 (1996) 713–726.

[12] Rhie, C. M., Chow, W. L., Numerical study of the turbulent flow past an airfoil with trailing edge separation, AIAA Journal 21 (11) (1983) 1 525–1 532.

[13] Vimmr, J., Jonášová, A., On the modelling of steady generalized Newtonian flows in a 3D coronary bypass, Engineering Mechanics 15 (3) (2008) 193–203.

[14] Vimmr, J., Jonášová, A., Non-Newtonian effects of blood flow in complete coronary and femoral bypasses, Mathematics and Computers in Simulation 80 (6) (2010) 1 324–1 336.